Available online at www.sciencedirect.com
SCIENCE DIRECT®
Journal of Sound and Vibration 286 (2005) 451–476
JOURNAL OF SOUND AND VIBRATION
www.elsevier.com/locate/jsvi

Adaptive autoregressive modeling of non-stationary vibration signals under distinct gear states. Part 2: experimental analysis

Y.M. Zhan, A.K.S. Jardine*

Department of Mechanical and Industrial Engineering, University of Toronto, 5 King's College Road, Toronto, Ont., Canada M5S 3G8

Received 26 January 2004; received in revised form 24 September 2004; accepted 6 October 2004
Available online 28 December 2004

Abstract

Parametric time–frequency representation based on parametric models is more desirable for presenting highly precise time–frequency domain information due to its high-resolution property. However, the sensitivity and robustness of parametric models, in particular the parametric models on the basis of advanced adaptive filtering algorithms, has never been investigated for on-line condition monitoring of rotating machinery. Part 1 of this study proposed three adaptive parametric models based on three advanced adaptive filtering algorithms. Part 2 of this study is concerned with the effectiveness of the proposed models under distinct gear states, especially the highly non-stationary conditions accrued from advanced gear faults. Four gear states are considered: healthy state, adjacent gear tooth failure, non-adjacent gear tooth failure and distributed gear tooth failure. The vibration signals used in this study include the time-domain synchronous averaging signal and gear motion residual signal for each considered gear state. The test results demonstrate that the optimum filter behavior can readily be attained and the white Gaussian assumption of innovations can relatively be easily guaranteed for the NAKF-based model under distinct gear states and a wide variety of model initializations. On the other hand, the EKF- and MEKF-based models are capable of generating more accurate time–frequency representations than the NAKF-based model, but in general the optimality condition for white Gaussian assumption cannot be guaranteed for these two advanced models. Therefore, the NAKF-based model is preferred for automatic condition monitoring due to its appealing robustness to distinct gear states and arbitrary model

*Corresponding author. Tel.: +1 416 978 2921; fax: +1 416 946 5462.
E-mail addresses: yimin.zhan@utoronto.cat (Y.M. Zhan), jardine@mie.utoronto.ca (A.K.S. Jardine).

0022-460X/$ - see front matter
doi:10.1016/j.jsv.2004.10.023

initializations, whereas the EKF- and MEKF-based models are desirable when accurate time–frequency representation is concerned.

1. Introduction

The objective of any manufacturing process is the efficient production of a part with specific shape with acceptable dimensional accuracy and quality. Deviation of the machine conditions from a prescribed plan may influence the final part quality and must be examined in detail by the experienced operator. Global competition and the current economic conditions have forced many manufacturing organizations to improve product quality and cut production costs at the same time. The requirements for increased plant productivity, safety, and reduced maintenance costs, have led to a growth in popularity of methods for condition monitoring to aid the planning of plant preventive maintenance and operational policies [1]. Increased use of automation, although reduces the burden on machine operators and the risk of human error, renders the production process more vulnerable to various kinds of faults.

However, in the applications of condition monitoring and fault diagnosis techniques to many mechanical systems, the component of interest is often inaccessible and cannot be observed or inspected directly. Therefore, to determine the condition of inaccessible components of an operating machine, the only possible course of action is to measure at a remote station some related signal, say vibration signals which carry a great deal of information describing the condition of the component. Hence, vibration monitoring presents a unique and appealing means to conduct condition monitoring and offers significant rewards due to economic benefits that accrue from its effectiveness. It has been investigated extensively in a wide variety of engineering maintenance literature. The well-known phrase 'running smoothly' reflects the fact that for a long time humans have monitored the condition of machines by monitoring the vibrations that they produce [2]. Condition monitoring of rotating machinery based upon vibration analysis belongs to the most sophisticated methods of quality control or quality assurance in connection with ISO-9000 standards and the method is widely applied, especially in the case of a high volume serial production [3].

In this area, generally speaking, development and investigation of time–frequency (T–F) analysis of rotating machinery subject to vibration monitoring attract most research interests. By means of T–F analysis, one is able to gain insight into the dynamics of the object of interest since it distinguishes itself from conventional spectral analysis like fast Fourier transform (FFT) by presenting time-varying power distribution over the T–F horizon. By using T–F analysis, one is able to localize the fault and evaluate its severity and thus it is critical for condition monitoring of rotating machinery. In this connection, parametric T–F representation based on parametric models is more desirable due to its high-resolution property.

However, up to now, there has not been a comprehensive investigation in which the effectiveness of parametric models based on advanced adaptive filtering algorithms is evaluated in T–F domain for on-line condition monitoring of rotating machinery, say, using the on-line vibration data measured under the highly non-stationary conditions caused by geometric

irregularities of gear profile and advanced gear faults. Such a study will be attempted here. In Part 1 of this paper, three adaptive parametric models are proposed and investigated using numerically generated test signals. The investigation presented in Part 2 is aimed at evaluating the performance of the proposed models in T–F domain using actual non-stationary gear vibration data. The T–F representations produced by each proposed model will be analyzed and a cross-section mean plot will be extracted from the dominant (fault-induced) energy region of each T–F map to assist the model performance analysis.

The remainder of this study is organized as follows. Section 2 discusses the experimental setup in which the mechanical diagnostic test bed utilized to provide gear vibration data will be described. Section 3 discusses the general signal processing policy in which the four distinct gear states will be introduced and the status of TSA and residual signals to be processed in this study will be explained; moreover, the signal processing policy and the criterion for evaluating the efficiency of the proposed models will be addressed in detail. Section 4 discusses the model identification. Section 5 presents the analysis results of the performance of the proposed three parametric models under four distinct gear states. Conclusions are given in Section 6.

2. Experimental setup

In order to investigate the performance of the proposed models on real condition monitoring signals, a mechanical diagnostics test bed (MDTB, cf. Fig. 1) was utilized in this study to provide data on a commercial transmission as its health progresses from new to faulted and finally to failure. The vibration data used in this study are obtained from the Applied Research Laboratory at the Pennsylvania State University [4]. The MDTB is functionally a motor-drive train-generator test stand [5]. The gearbox is driven at a set input speed using a 30 horsepower (hp), 1750 rev/min AC drive motor, and the torque is applied by a 75 hp, 1750 rev/min AC absorption motor. The maximum speed and torque are 3500 rev/min and 225 ft lb, respectively. The speed variation can

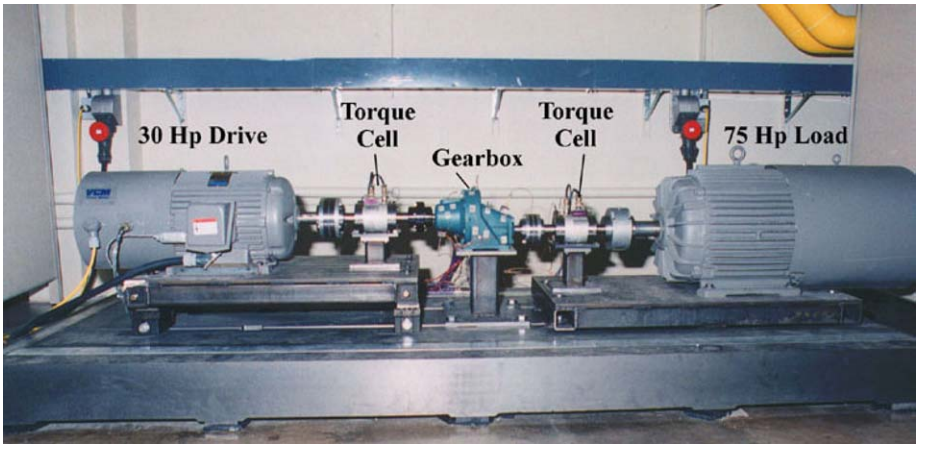

Fig. 1. Mechanical diagnostic test bed.

Table 1
Gearbox specifications of TR#10, TR#7, TR#8 and TR#6

Gearbox ID#	DS3S0150XX
Make	Dodge APG
Model	R86001
Rated input speed	1750 rev/min
Maximum rated output torque	528 in lb
Maximum rated input (hp)	10.0
Gear ratio	1.533
Contact ratio	2.388
Gear mesh frequency of driven gear (Hz)	875.53
Gear mesh frequency of pinion gear (Hz)	874.99
Number of teeth (driven gear)	46
Number of teeth (pinion gear)	30

be accomplished by varying the frequency to the motor with a digital vector drive unit. However, in this test run, the shaft speed is kept constant at 1750 rev/min. The variation of the torque is accomplished by a similar vector unit capable of controlling the current output of the absorption motor. The system speed and torque set points are produced by analog input signals (0–10 VDC) supplied by the data acquisition (DAQ) computer and a D/A board. The MDTB is highly efficient because the electrical power that is generated by the absorber is fed back to the driver motor. The mechanical and electrical losses are sustained by a small fraction of wall power. The MDTB has the capability of testing single and double reduction industrial gearboxes with ratios from about 1.2:1 to 6:1. The gearboxes are nominally in the 5–20 hp range. The system is sized to provide the maximum versatility to speed and torque settings. The motors provide about 2 to 5 times the rated torque of the selected gearboxes, and thus the system can provide good overload capability. The use of different reduction ratios and gearboxes than listed above is possible if appropriate consideration to system operation is given. The motors and gearbox are hard-mounted and aligned on a bedplate. The bedplate is mounted using isolation feet to prevent vibration transmission to the floor. The shafts are connected with both flexible and rigid couplings. Torque limiting clutches are used on both sides of the gearbox to prevent the transmission of excessive torque as could occur with gear jam or bearing seizure. In addition, torque cells are used on both sides of the gearbox to directly monitor the efficiency and the loads transmitted [5]. The general gearbox information is shown in Table 1.

3. Signal processing policy

The test runs used in this study include TR#10, TR#7, TR#8 and TR#6 [4], in which TR is the abbreviation of test run and the number is the sequence code of a test run. The test runs were conducted with identical single reduction helical 1:1.5 ratio gearboxes which were run at 100% output torque and hp for 96 h then increased to 200% or 300% torque and hp until failure for a number of hours. For each test run, there is a number of data files collected with unequal inspection intervals during the lifetime of gearbox. Each data file was collected in 10 s windows, which cover 200,000 sampling points in total and triggered by accelerometer RMS thresholds. The

Table 2
Two operating conditions of TR#10, TR#7, TR#8 and TR#6[a]

Condition	Input speed (rev/min)	Output torque (in lb)	Power (hp)	Duration (h)
#1	1750	540	9.8	96.0
#2	1750	1080/1080/1080/1620	20/20/20/30	93.25/38.50/51.50/6.00

[a]Output torque (in lb) 1080/1080/1080/1620 denotes the loads for test-runs TR#10, TR#7, TR#8 and TR#6, respectively. Same for power (hp) and duration (h). The TSA and residual signals of TR#10 analyzed in this study are sampled under condition #1, while the signals of TR#7, TR#8 and TR#6 analyzed in this study are sampled under condition #2.

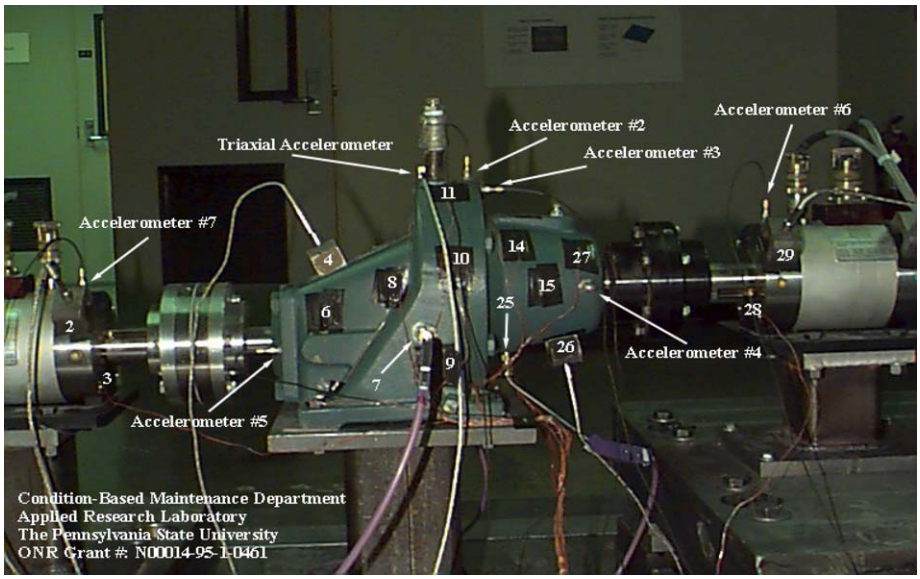

Fig. 2. Locations of sensors.

sampling frequency is 20 kHz. Table 2 gives a brief description of the two operating conditions of the four test runs used in this study. The following data are contained in each test run: single axis accelerometer sensor (A02-A07), triaxial accelerometer (A10: axial; A11: || floor; A12: perp floor), external microphone sensor (M01). Fig. 2 shows the locations of sensors. Data collected by the single axis shear piezoelectric accelerometer A03 for axial direction is selected in this study. To investigate the performance of the proposed three models, four distinct gear states: (a) healthy gear (TR#10); (b) adjacent gear tooth failure (TR#7); (c) two non-adjacent gear tooth failure (TR#8); and (d) distributed gear tooth failure (TR#6), are considered in this study. Fig. 3 shows the state of the driven gear under which the vibration signals were measured and analyzed in this study.

The time-domain signals used in this study involve the time-domain synchronous average (TSA) and corresponding residual signals obtained by the elimination from the FFT spectrum of

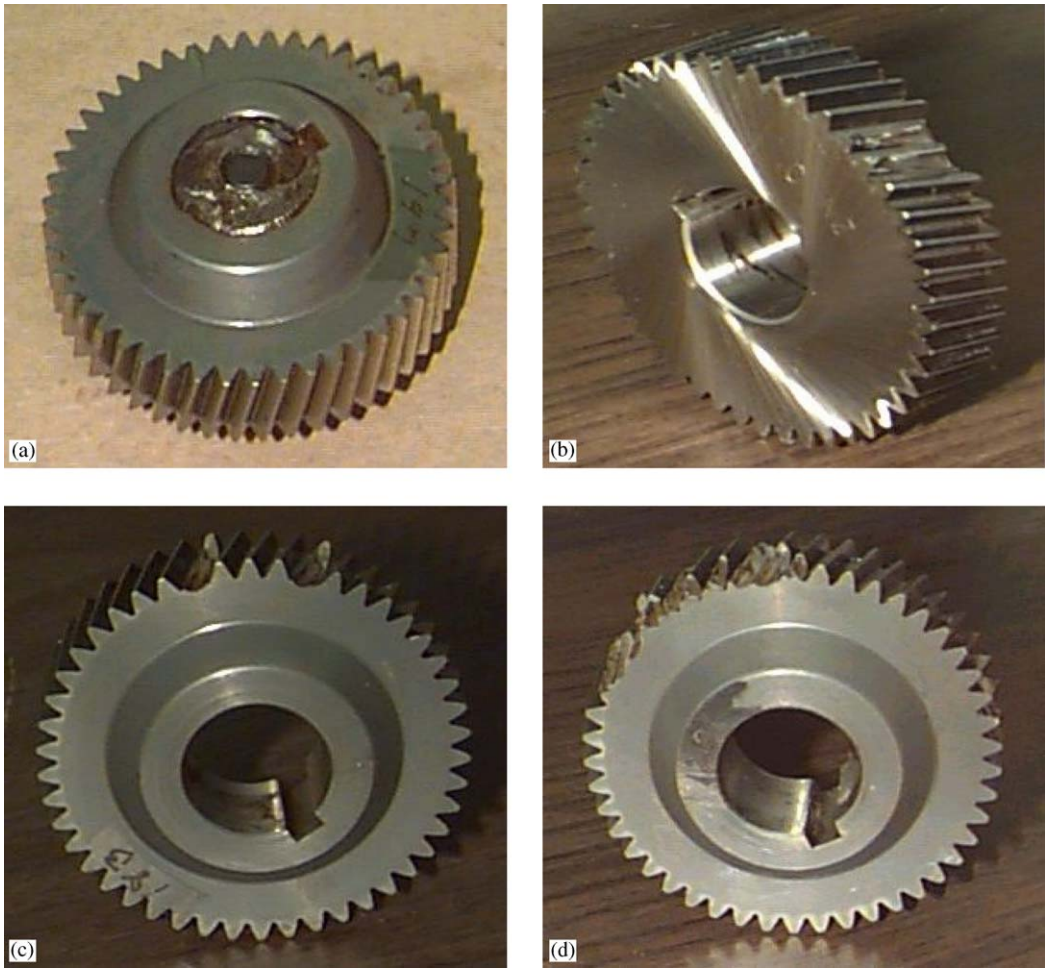

Fig. 3. States of the driven gears under which the vibration signals analyzed in this study were measured. (a) Healthy gear (TR#10), (b) adjacent gear tooth failure (TR#7), (c) non-adjacent gear tooth failure (TR#8), (d) distributed gear tooth failure (TR#6).

TSA signal of the fundamental and harmonics of the tooth-meshing frequency and ghost components and in the subsequent inverse Fourier transform and then reconstructing in the time-domain the remaining signal [6]. A critical investigation using TSA and residual signals of the healthy driven gear is first of all provided as a reference. The results presented here are based on extensive tests for the sake of obtaining as precise as possible T–F representations. The gear of interest is always the driven gear since its failure is the major factor which caused the test rig to shut down. Since the raw data indicates that a significant number of sampling points (>10) were discarded at the 1 s boundaries ($n \times 20{,}000$ samples) in the data files of TR#7, TR#8 and TR#6, i.e. between the end of 1 s and the start of the next, the original 200,000 points of 10 s is divided into 10 1 s segments of equal length, each of which contains 20,000 points. Since the meshing frequency f_{gearmesh} is 875.53 Hz and the number of teeth of driven gear is 46, the shaft rotating

frequency of the driven gear is then 19.033 Hz. Therefore, only 19 revolutions in each 20,000 points segment are available to yield one TSA signal. A proper one of the resulting 10 TSA signals is selected for conducting the following analysis. The problem that skipped seconds are contained in the 10 s windows was eliminated in TR#10. It therefore allows 190 revolutions to be averaged in TR#10 to obtain a TSA signal with a fairly efficient reduction of background noise.

Two kinds of analysis, using TSA and residual signals, respectively, are conducted for each test run. The time-domain TSA or residual signal is placed to be with the resulting T–F maps for the sake of presenting a convenient reference. The frequency range of all T–F maps considered in this study is $[0, 4 \times f_{\text{gearmesh}}]$, where the frequency resolution is 10.006 Hz and angular resolution is 0.3425° which corresponds to 1051 data points sampled over one entire revolution of the driven gear.

It should be emphasized that, unlike non-parametric T–F techniques, i.e. STFT or wavelet, the parametric T–F representation possesses considerably high resolution and therefore presents quite distinctive discrimination between actual and spurious frequency components which, however, reduces the visibility of fault-induced feature in T–F domain if visual inspection is attempted, whereas the non-parametric transforms are able to present some dominant energy congregation patches incurred by fault over the T–F horizon. This feature is particularly notable when residual signal is analyzed. However, for TSA signal the fault-induced impulses modulate the meshing fundamental and its harmonics which are dominant components of gear motion spectrum and therefore cover a wide frequency band. Thus, to be consistent with the objective of fault diagnosis, a frequency band-averaged cross-section mean plot that is normalized between [0, 1] to reduce the variation among different signatures is provided to furnish an auxiliary tool for evaluating the efficiency of proposed models for each TSA or gear motion residual signal within the band which contains the most dominant fault-induced feature. This is similar to the well-known narrowband amplitude and phase demodulation technique [7] where the TSA signal is band-pass filtered in the frequency domain around one of the strongest meshing harmonics with a bandwidth comprising a meaningful number of its sidebands. In the meantime, the STFT is chosen to provide a reference cross-section mean plot by taking spectral average within the same frequency band over the entire revolution for each TSA or residual signal since it possesses a uniform T–F resolution which is therefore comparable with the cross-section mean plots of the proposed parametric models. On account of this consideration, the T–F maps produced by STFT will be presented for all TSA and residual signals in this study so as to assist the analysis.

The efficiency of each model is concluded mainly based on

(1) the T–F map and,
(2) the frequency band-averaged cross-section mean plot of each model.

The criterion for evaluating the efficiency of each model is to examine

(1) the resolution and accuracy of the resulting T–F representation and,
(2) how significantly the fault-induced feature is presented in the resulting cross-section mean plot of each model.

The second criterion is conducted with the aid of a comparison with the corresponding cross-section mean plot of STFT. We simply take the same means as the one used by Wang et al. [8] to

Table 3
Generalization of model evaluation using gearbox vibration signals[a]

Test run	Signal	Model	Order p	K–S test	Pr (%)	Zero mean test of innovations			
						[0°, 180°]	[180°, 360°]	[360°, 540°]	[540°, 720°]
TR#10	TSA	I	70	0	1.14	—			
		II		1	77.88	2.4512e-03	1.4181e-03	1.2476e-03	1.5191e-03
		III		1	77.50	2.3468e-03	1.4845e-03	1.2336e-03	1.4896e-03
	RES	I	170	0	2.00	—			
		II		0	27.45	2.4414e-04	8.2699e-05	5.8755e-05	4.7754e-05
		III		0	29.36	2.8839e-04	1.2282e-04	6.8852e-05	5.3865e-05
TR#7	TSA	I	70	0	1.24	—			
		II		1	18.21	7.4842e-03	1.0368e-03	2.7051e-03	2.9521e-03
		III		0	21.45	5.4811e-03	8.3651e-04	2.4261e-03	2.7006e-03
	RES	I	170	1	1.91	—			
		II		1	8.39	2.1004e-03	2.6677e-04	1.9043e-04	1.2917e-04
		III		1	7.63	2.1068e-03	2.8144e-04	1.9467e-04	1.3526e-04
TR#8	TSA	I	70	0	1.81	—			
		II		0	21.54	1.0417e-02	1.8785e-03	1.1171e-03	1.1469e-03
		III		1	30.98	1.7661e-02	6.3903e-03	4.4088e-03	2.7492e-03
	RES	I	170	0	2.96	—			
		II		0	10.01	2.3601e-03	6.8948e-04	4.0448e-04	2.7289e-04
		III		0	10.68	2.3623e-03	6.7493e-04	4.6656e-04	3.2618e-04
TR#6	TSA	I	70	1	2.19	—			
		II		1	9.15	1.0492e-02	4.5268e-03	4.1570e-03	5.0918e-03
		III		1	10.01	2.3195e-02	1.2673e-02	7.9669e-03	7.1522e-03
	RES	I	170	1	2.96	—			
		II		1	5.72	7.9919e-03	5.8221e-04	2.9925e-04	1.3085e-04
		III		1	5.62	7.9727e-03	5.2211e-04	2.8882e-04	1.2173e-04

[a]RES denotes the residual signal. K–S test denotes the Kolmogorov–Smirnov goodness-of-fit test, where 0 denotes that the null hypothesis that innovations can be adjusted to Gaussian distribution is accepted under 5% significance level and 1 denotes rejection of null hypothesis. Each TSA or residual signal is processed twice in a recursive fashion and thus the zero mean test of innovations covers two revolutions from 0° to 720°.

Table 4
Generalization of model efficiency under distinct states of gearbox[a]

Test run	Signal	NAKF-based model I	EKF-based model II	MEKF-based model III
TR#10	TSA	CI	CI	CI
	RES	CI	CI	CI
TR#7	TSA	CI	CI	CI
	RES	CI	CI	CI
TR#8	TSA	SI	CI	CI
	RES	CI	CI	CI
TR#6	TSA	CI	CI	CI
	RES	CI	CI	CI

[a]CI denotes "clear indication", SI denotes "some indication".

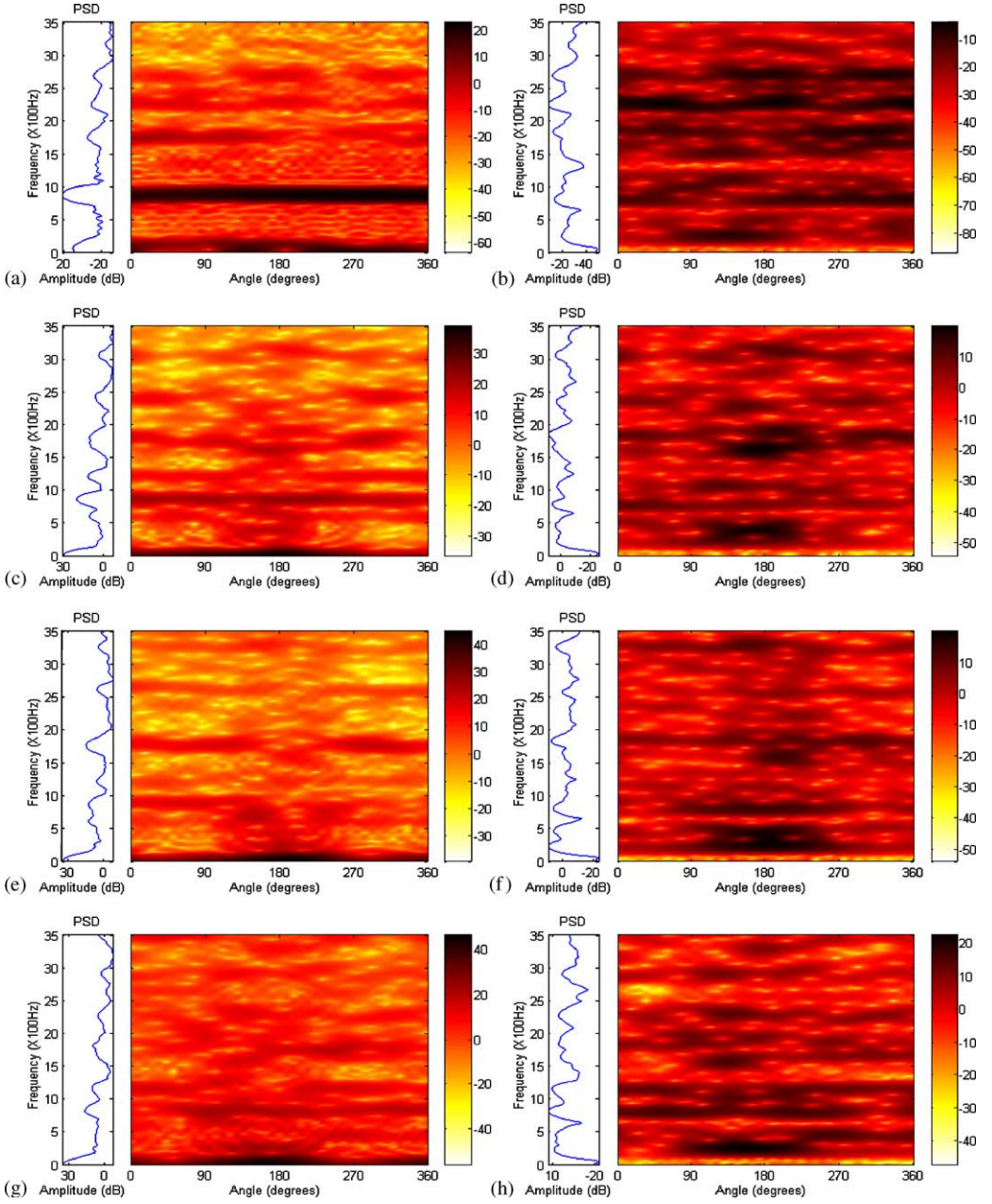

Fig. 4. T–F maps of TSA and residual signals by STFT, where the frequency resolution is 10.006 Hz and the time resolution is 9°. (a) T–F map of TSA signal (TR#10), (b) T–F map of residual signal (TR#10), (c) T–F map of TSA signal (TR#7), (d) T–F map of residual signal (TR#7), (e) T–F map of TSA signal (TR#8), (f) T–F map of residual signal (TR#8), (g) T–F map of TSA signal (TR#6), (h) T–F map of residual signal (TR#6).

generalize the results. The symbol CI means that there is a clear indication of the state of driven gear in comparison to the cross-section mean plot of STFT. SI denotes that there exists some, but not a definite indication of gear state or usually fault-induced feature and thus further analysis is needed to confirm this diagnosis result. NI means that there is no clear indication of the expected gear state feature.

It should be noted that a complete consistency between the STFT cross-section mean plot and the parametric cross-section mean plot is unlikely to be obtained since the STFT, as a non-parametric T–F technique, is a low-resolution method, whereas the parametric models are high-resolution ones. As well, the parametric models with the aid of an adaptive estimation of the noise covariance are able to effectively fit the true underlying process. As such, the resulting T–F representations should in some extent differ from the ones produced by non-parametric T–F techniques. Hence, the assessment of model performance in the following text will only focus on the general presence of the fault-induced feature.

Further, it is found that a set of good model parameters that enables the model satisfy the optimality checks described in Part 1 of this study cannot guarantee the accuracy of the resulting T–F representation. Therefore, to obtain a desirable and accurate T–F representation is the predominant objective for selecting model parameters.

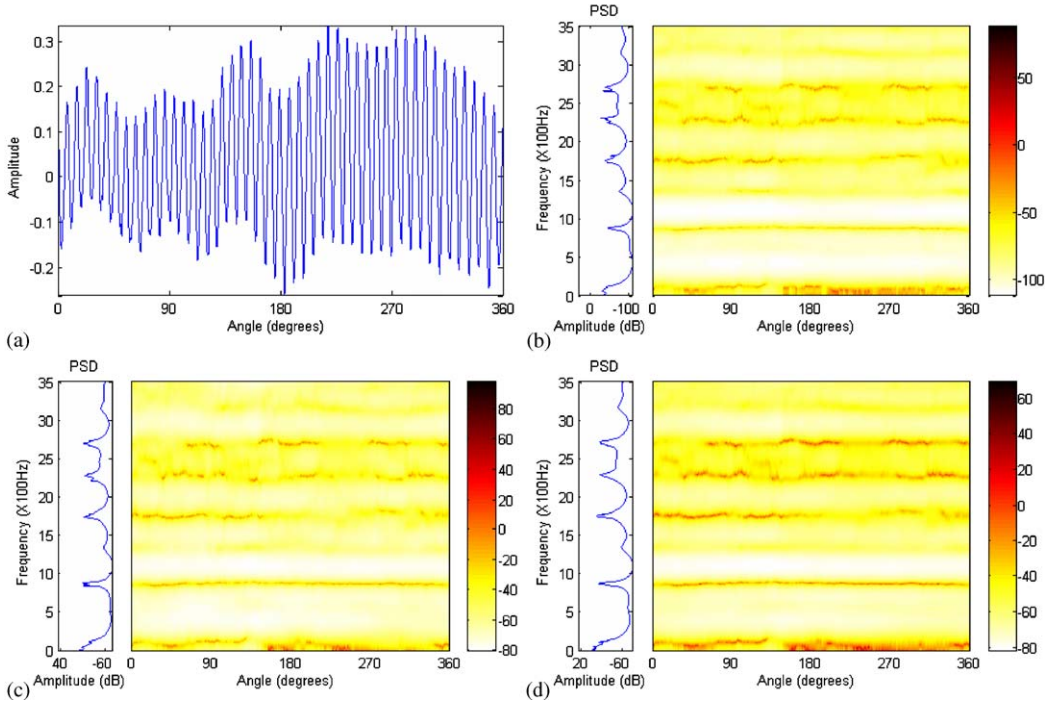

Fig. 5. TSA signal of the driven gear under healthy state and T–F maps, where the TSA signal is obtained from TR#10, and the number of averaged revolutions is 190. (a) TSA signal under healthy state, (b) T–F map of model I (NAKF), (c) T–F map of model II (EKF), (d) T–F map of model III (MEKF).

4. Model identification

Strictly speaking, the model order should be time-dependent variable even within one revolution of the gear of interest since the time-varying (or T–F) representation is considered for each revolution. Obviously, this is not a realistic consideration for real-time applications and automatic condition monitoring due to the tremendous computational load induced by such a scheme. Therefore, a constant model order must be employed within each revolution. On the other hand, a constant model order is also highly desirable throughout each test run for automatic condition monitoring and real-time applications. In fact, this is a compulsory requirement due to a number of factors. First, as pointed out in Section 2.5 of Part 1 of this study, the available model order selection criteria can only be used as a guide only, subjective assessment must be involved into the determination of model order and thus is not applicable for automatic condition monitoring and real-time applications. Second, the intensive computational load induced by estimation of 'optimum' model order during each inspection will inevitably harm the real-time applications. Third, the NAKF-based time-varying AR model has been tested using extensive different vibration data, always with acceptable results under a wide selection range of model order. Therefore, a constant model order throughout each test run is necessary and applicable. As well, since the three state space models are transformed from the identical time-varying AR model, it is natural to assign the EKF- and MEKF-based models the same order value as the one used by the NAKF-based model. By doing so, it is indeed equivalent to assuming that the

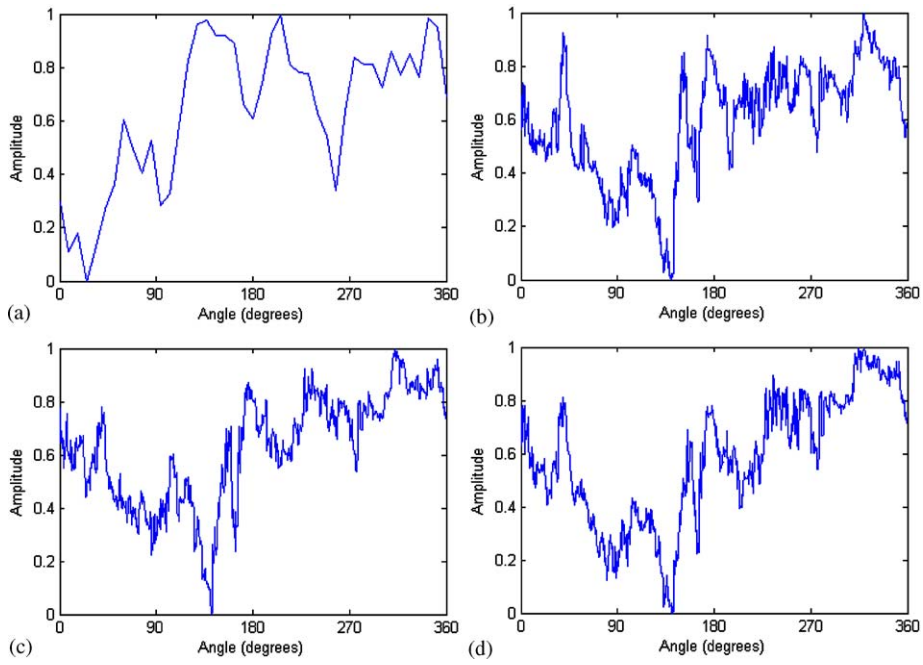

Fig. 6. Normalized cross-section mean plots of STFT and proposed models for the TSA signal in Fig. 5(a), where the averaged frequency band is $[0, 4 \times f_{\text{gearmesh}}]$ Hz. (a) Cross-section mean of STFT, (b) cross-section mean of model I (NAKF), (c) cross-section mean of model II (EKF), (d) cross-section mean of model III (MEKF).

selection of model order is independent of the evolution laws of the state vector. This was confirmed by the model evaluation using simulated signals in Part 1 of this study and also our extensive experiments using various on-line gearbox vibration signals.

In view of the above considerations, a constant model order is assigned to each of the three parametric models when TSA or gear motion residual signal is analyzed. Order values of 70 and 170 are finally determined for TSA and gear motion residual signals, respectively, as shown in Table 3. The results of optimality tests for white Gaussian assumption and zero mean of innovations under the selected model orders are generalized in Table 3. The evaluation of model efficiency is summarized in Table 4.

To focus on the T–F analysis, the presentation of model order selection procedure, normal probability plot and zero mean test of innovations is ignored in this study. The reader is referred to the same model order selection procedure as described in Part 1 of this paper using simulated signals, and to the Appendix A at the end of Part 1 of this paper for the introduction of Kolmogorov–Smirnov (K–S) goodness-of-fit test. The T–F maps, produced by STFT for comparison purpose, of the same TSA and gear motion residual signals that will be examined by the proposed three parametric models in the next section are presented in Fig. 4.

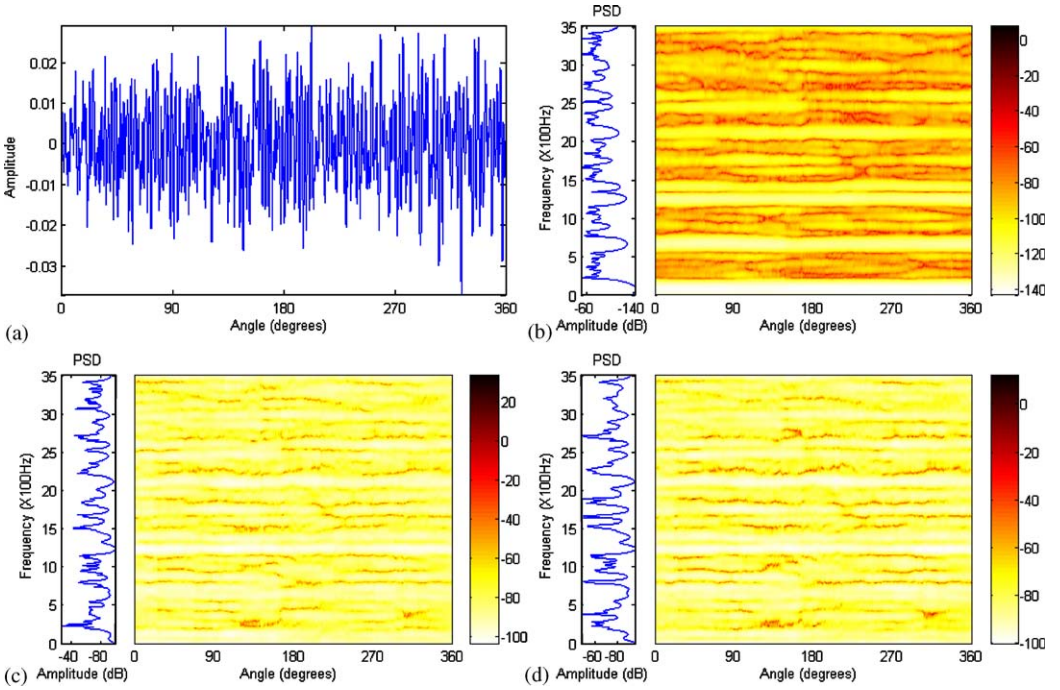

Fig. 7. Residual signal of the driven gear under healthy state and T–F maps, where the residual signal is extracted from the TSA signal in Fig. 5(a). (a) Residual signal under healthy state, (b) T–F map of model I (NAKF), (c) T–F map of model II (EKF), (d) T–F map of model III (MEKF).

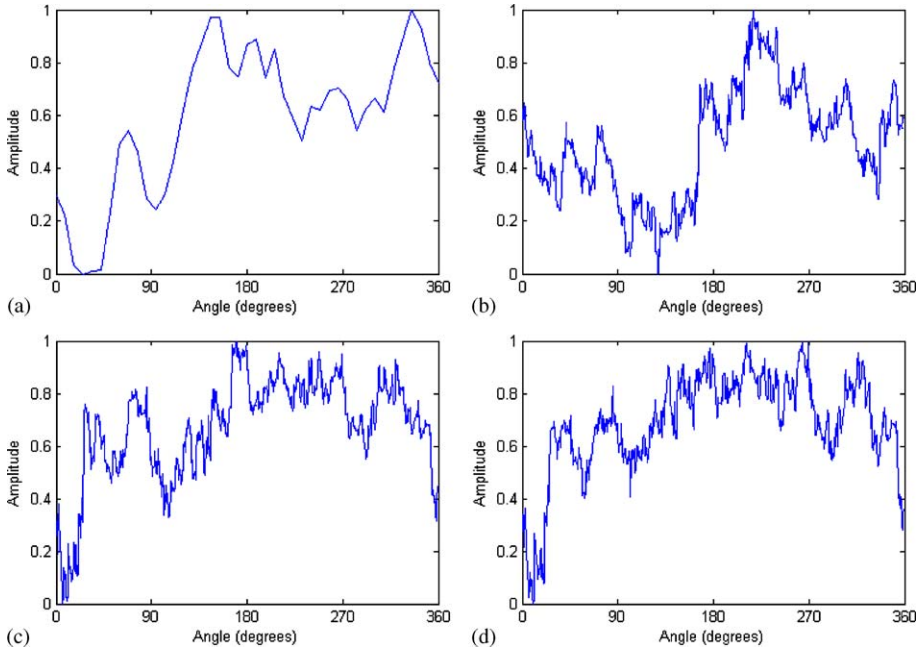

Fig. 8. Normalized cross-section mean plots of STFT and proposed models for the residual signal in Fig. 7(a), where the averaged frequency band is $[0, 4 \times f_{\text{gearmesh}}]$ Hz. (a) Cross-section mean of STFT, (b) cross-section mean of model I (NAKF), (c) cross-section mean of model II (EKF), (d) cross-section mean of model III (MEKF).

5. Analysis of results

5.1. Healthy gear (TR#10)

First, as a reference, signal collected from the gearbox of TR#10 under healthy state is analyzed. The TSA signal as shown in Fig. 5(a) is obtained by taking average of 190 revolutions and achieves a very effective noise removal and clearly shows 46 peaks corresponding to 46 tooth periods, where an apparent increase in the vibration amplitude starting from 140° due to the geometric irregularities of the gear profile can be observed. It is therefore expected to see an energy increase after 140° in the resulting T–F representation of this TSA signal. Figs. 5(b), (c) and (d) present the T–F maps produced by models I, II and III, respectively. It can be seen that the energy is mainly centered around the meshing fundamental at 875.53 Hz and its first two harmonics as indicated by the rightmost PSD plots of all three maps, which in this case are also the dominant meshing frequencies. Generally speaking, all three maps present a great consistency in clearly highlighting the meshing fundamental and its harmonics and possibly some ghost components at 2300 Hz and some low-level components which may include modulation sidebands and low-order harmonics of the shaft rotation frequency. Further investigation indicates that the T–F maps of these three models are well consistent with the one produced by STFT as shown in Fig. 4(a).

Fig. 6 presents the cross-section mean plots of STFT and the parametric models over the full considered frequency band $[0, 4 \times f_{\text{gearmesh}}]$. As shown in Figs. 6(b)–(d) all models present higher

energy level within the angular interval [140°, 360°] than the interval [0°, 140°]. These results are consistent with the cross-section mean plot of STFT as shown in Fig. 6(a) and also consistent with the previous analysis of the TSA signal. The only notable difference between the cross-section mean plots of the three parametric models and that of STFT exists within the angular interval [0°, 140°], in which they show different traces along the angular axis. However, it is reasonable to believe that the plots of these three parametric models are more accurate (CI) than that of STFT. This is due to such a fact that the TSA signal has a periodic feature and repeats itself from one revolution to the next and thus, the energy levels at two end angular positions, e.g. 0° and 360°, should be very close to each other. Apparently, the cross-section mean plots of the three parametric models are in accordance with such a fact, but the cross-section mean plot of STFT as shown in Fig. 6(a) is not.

Fig. 7(a) shows the gear motion residual signal extracted from the TSA signal in Fig. 5(a) by eliminating dominant meshing fundamental and its harmonics and ghost components, which thereby increases the proportion of the energy in the remaining signal which is related to the damage and so increases the sensitivity to small energy changes related to the damage. The T–F maps of the residual signal are presented in Figs. 7(b)–(d). As can be seen, more low-level frequency components emerge in each T–F map after the removal of dominant DC components. Due to the gear geometric irregularities caused possibly by misalignment, eccentricity and other deviations from the ideal profile of gear, modulation effects, albeit small and local, become more

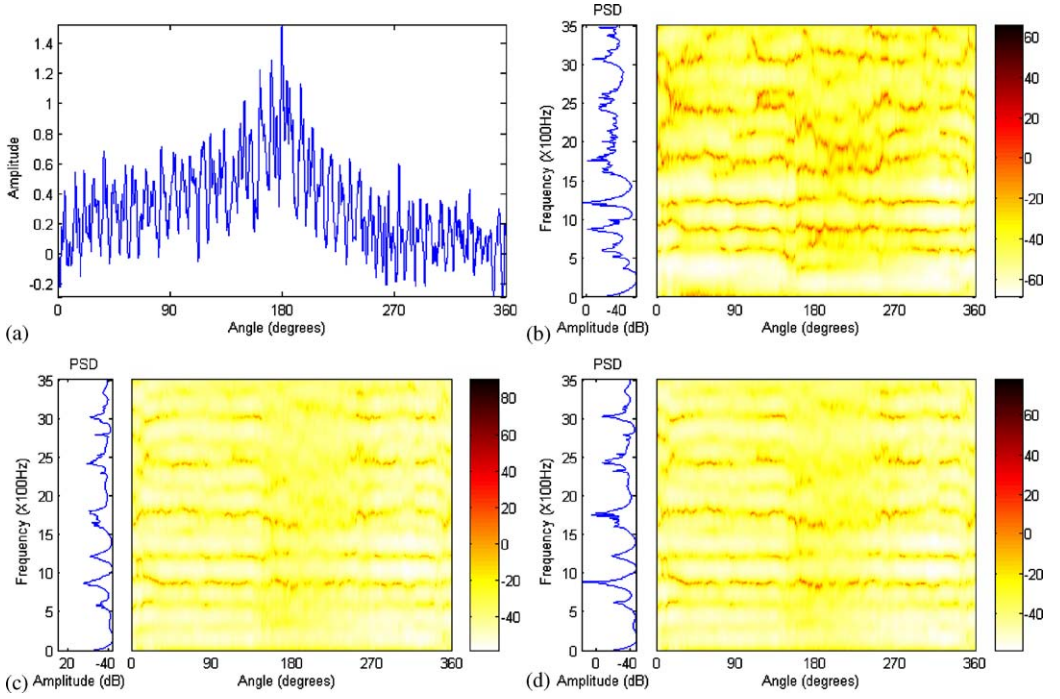

Fig. 9. TSA signal of the driven gear under the faulty state of two adjacent broken teeth and T–F maps, where the TSA signal is obtained from TR#7, and the number of averaged revolutions is 19. (a) TSA signal under faulty state, (b) T–F map of model I (NAKF), (c) T–F map of model II (EKF), (d) T–F map of model III (MEKF).

evident and appear in the traces of spectral contents along the angular axis in all three maps. Such imperfections are inevitable and a robust diagnostic technique should be insensitive to these small fluctuations [8].

Since the residual signal is obtained under the healthy state of the driven gear where the gear meshing fundamental and its harmonics and some ghost components have been digitally filtered out by putting to zero, the T–F representation is therefore expected to approximately have a uniform distribution of energy over the T–F horizon. Thus, the corresponding cross-section mean plot is obtained by taking spectral average over the full considered frequency range [0, $4 \times f_{\text{gearmesh}}$]. The results are presented in Fig. 8. As seen in Figs. 8(c) and (d), the cross-section mean plots of both model II and III show strong consistency with that of STFT in Fig. 8(a). Model I shows different power estimation within the angular interval of [0°, 30°]. However, this does not affect the presence of energy increase approximately from the angular interval [0°, 160°] to [160°, 360°]. Therefore, all models demonstrate similar energy distribution over one entire revolution and clearly indicate (CI) an energy distribution which is generally consistent with that of STFT.

5.2. *Faulty gears*

Three different failure modes of the driven gear, adjacent gear tooth failure (TR#7), two non-adjacent gear tooth failures (TR#8) and distributed gear tooth failure (TR#6), will be investigated in this section. It is pointed out in the original notations of data CDs that only 19 revolutions

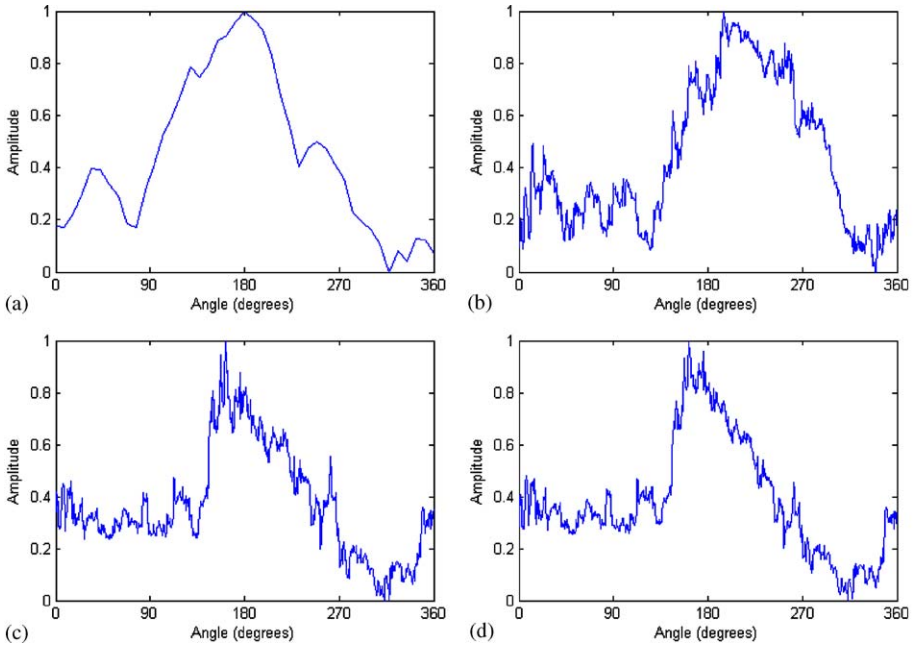

Fig. 10. Normalized cross-section mean plots of STFT and proposed models for the TSA signal in Fig. 9(a), where the averaged frequency band is [300, $4 \times f_{\text{gearmesh}}$] Hz. (a) Cross-section mean of STFT, (b) cross-section mean of model I (NAKF), (c) cross-section mean of model II (EKF), (d) cross-section mean of model III (MEKF).

maximum can be averaged to obtain one TSA signal in each of TR#7, TR#8 and TR#6 and it will thus result in 10 TSA signals for each data file and a low-level reduction of background white Gaussian noise. Therefore, in order to facilitate the visual inspection, the TSA signals with the damaged teeth close to 180° of the angular axis are selected. In this way, changes in the T–F maps are expected to occur around the middle of the angular axis. The corresponding residual signals are obtained in the same manner as aforementioned. Similar to the case of healthy gear, the following analysis will be presented using both TSA and residual signals.

5.2.1. *Adjacent gear tooth failure (TR#7)*

Figs. 9 and 10 show the analysis results of the adjacent gear tooth failure using TSA signal. Due to insufficient averaging, evident indication of disturbances caused by background noise can be observed in Fig. 9(a). The adjacent faulty teeth are located within the angular interval [130°, 200°]. Significant fault-induced modulation effects within the angular interval [130°, 250°] can be detected by visual inspection in all T–F maps as shown in Figs. 9(b)–(d). It is noteworthy that the prominence of fault-induced effects in parametric T–F maps would not be as apparent as those presented in non-parametric maps by means of visual observation since the parametric techniques have a data-adaptive feature, whereas the running time window employed by STFT, which covers a certain signal length in the time domain, will bring the fault-induced feature to adjacent angular

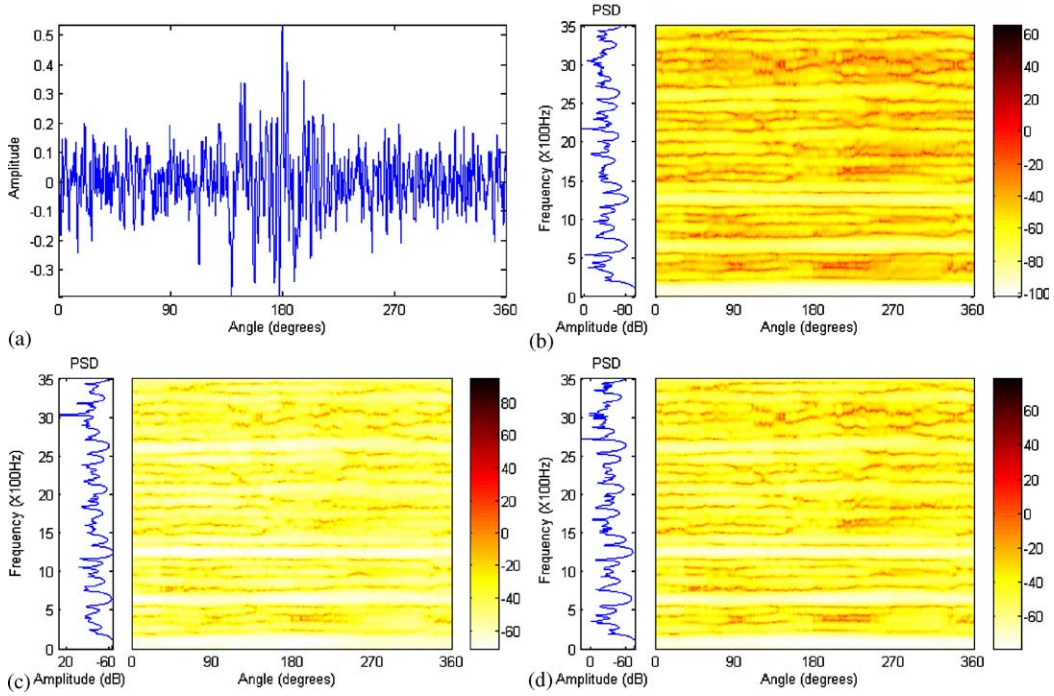

Fig. 11. Residual signal of the driven gear under the faulty state of two adjacent broken teeth and T–F maps, where the residual signal is extracted from the TSA signal in Fig. 9(a). (a) Residual signal under faulty state, (b) T–F map of model I (NAKF), (c) T–F map of model II (EKF), (d) T–F map of model III (MEKF).

positions where the faulty gear teeth are actually not involved in the meshing motion. Thus, the fault-induced effects will spread over an extended region in non-parametric T–F maps by using moving windows, whereas in parametric T–F maps these effects are specified at some T–F points where the abrupt changes of spectral contents take place. Therefore one may not expect to see some apparent dark patches in the T–F maps of parametric models. Specifically, the prominence of fault-induced transient effects is obscured by the dominant meshing frequencies of TSA signal.

The cross-section mean plots computed over the frequency band [300, $4 \times f_{\text{gearmesh}}$] Hz are presented in Fig. 10. All models clearly indicate (CI) the power distributions which are generally consistent with that of STFT as shown in Fig. 10(a), where model I shows a slight delay in highlighting the energy peak in comparison with models II and III.

The analysis using the gear motion residual signal extracted from the TSA signal in Fig. 9(a) is presented in Figs. 11 and 12. The two adjacent tooth cracks-induced modulation effects can clearly be observed within the angular interval [130°, 200°] in Fig. 11(a). The three models produce similar T–F representations as shown in Figs. 11(b)–(d).

The T–F analysis by means of STFT as shown in Fig. 4(d) indicates that the most dominant region which highlights the fault-induced feature over the T–F horizon lies in the frequency band [1500, 2000] Hz. The cross-section mean plots of STFT and the three parametric models are therefore obtained by taking spectral average over the frequency band of [1500, 2000] Hz and

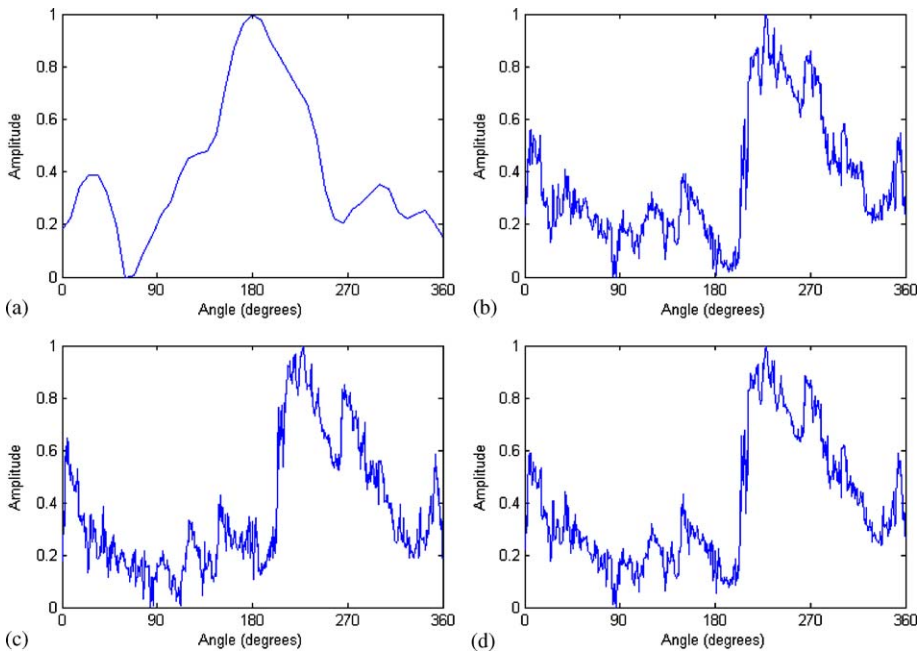

Fig. 12. Normalized cross-section mean plots of STFT and proposed models for the residual signal in Fig. 11(a), where the averaged frequency band is [1500,2000] Hz. (a) Cross-section mean of STFT, (b) cross-section mean of model I (NAKF), (c) cross-section mean of model II (EKF), (d) cross-section mean of model III (MEKF).

presented in Fig. 12. As can be seen, there is a phase lag of about 45° in the presence of the dominant energy region in Figs. 12(b), (c) and (d), respectively. However, such a lag does not affect the presence of fault-induced feature. All models clearly indicate the fault-induced feature around 225° (CI).

5.2.2. *Non-adjacent gear tooth failure (TR#8)*

Figs. 13 and 14 present the results for the gearbox which was shutdown due to two non-adjacent gear tooth failures, using the TSA signal. Apparent irregularities between [140°, 250°] can be identified from the TSA trace as shown in Fig. 13(a). The resulting T–F maps are shown in Figs. 13(b)–(d), where evident modulation effects can be detected within the angular interval [140°, 250°] in each T–F map.

The cross-section mean plots of this TSA signal illustrate that models II and III yield the most prominent indication (CI) of fault-induced feature within [140°, 250°], as shown in Figs. 14(c) and (d). The energy valley between [140°, 250°] is well consistent with the angular distance between these two non-adjacent faulty teeth. However, as shown in Fig. 14(b), model I shows slightly low estimation within the angular interval [140°, 190°] which is not consistent with the estimation in the same region of the cross-section mean plots of STFT and models II and III as shown in

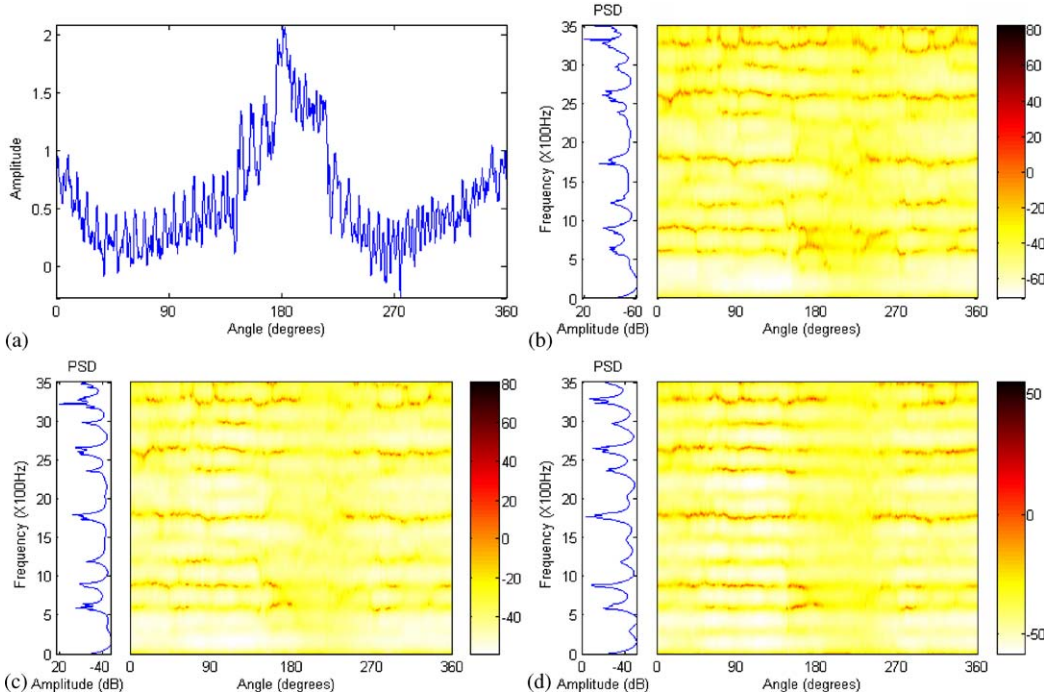

Fig. 13. TSA signal of the driven gear under the faulty state of two non-adjacent broken teeth and T–F maps, where the TSA signal is obtained from TR#8, and the number of averaged revolutions is 19. (a) TSA signal under faulty state, (b) T–F map of model I (NAKF), (c) T–F map of model II (EKF), (d) T–F map of model III (MEKF).

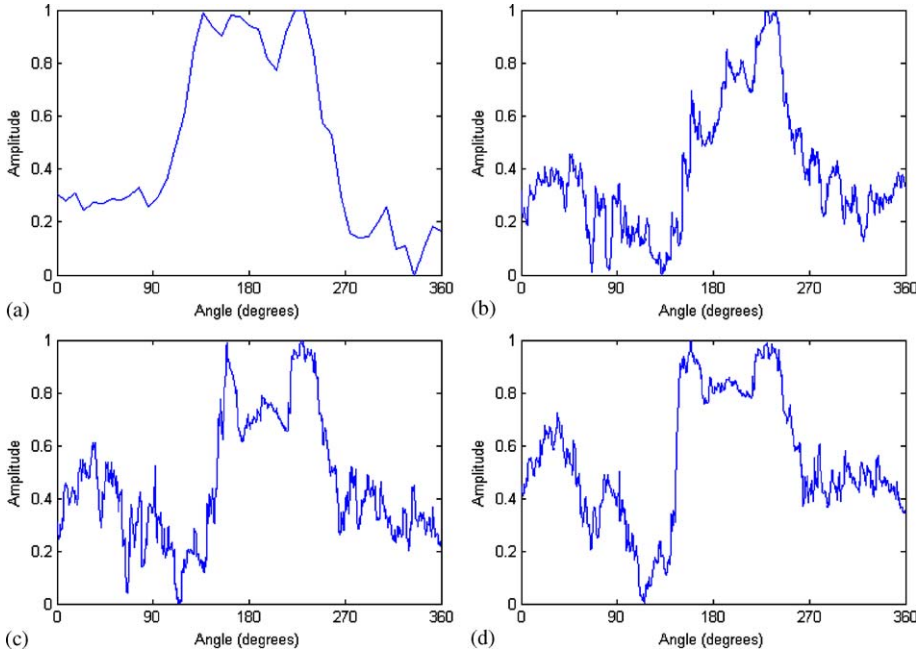

Fig. 14. Normalized cross-section mean plots of STFT and proposed models for the TSA signal in Fig. 13(a), where the averaged frequency band is [200, $4 \times f_{\text{gearmesh}}$] Hz. (a) Cross-section mean of STFT, (b) cross-section mean of model I (NAKF), (c) cross-section mean of model II (EKF), (d) cross-section mean of model III (MEKF).

Figs. 14(a), (c) and (d) respectively. Extensive tests were carried out. However, the estimation within this angular interval by model I cannot be as high as those of STFT and models II and III. Thus, to a small extent, it attenuates the presence of fault-induced feature (SI) in the T–F map of model I in this case.

The analysis using gear motion residual signal under this faulty state is presented in Figs. 15 and 16. The residual signal, as shown in Fig. 15(a), presents significant irregularities within the angular interval [140°, 250°]. The resulting T–F maps produced by the three parametric models, as shown in Figs. 15(b), (c) and (d) respectively, show a strong consistency with respect to the T–F distribution of this residual signal.

T–F analysis based on STFT denotes that frequency band [200, 600] Hz is the dominant region which contains the most significant fault-induced feature as shown in Fig. 4(f). Thus, the cross-section mean plots presented in Fig. 16 are obtained by taking spectral average over the frequency band [200, 600] Hz. It is clear that all the cross-section mean plots clearly indicates (CI) the feature induced by the two non-adjacent gear tooth failures in the middle of the revolution, in which the energy valley around 180° is exactly corresponding to the phase difference between the two peaks caused by the two non-adjacent tooth cracks as shown in Figs. 16(b), (c) and (d), respectively. However, the cross-section mean plot of STFT fails to reveal the fault-induced feature as shown in Fig. 16(a). Further inspection on Figs. 16(b)–(d) indicates that the energy valley at 180° is at an

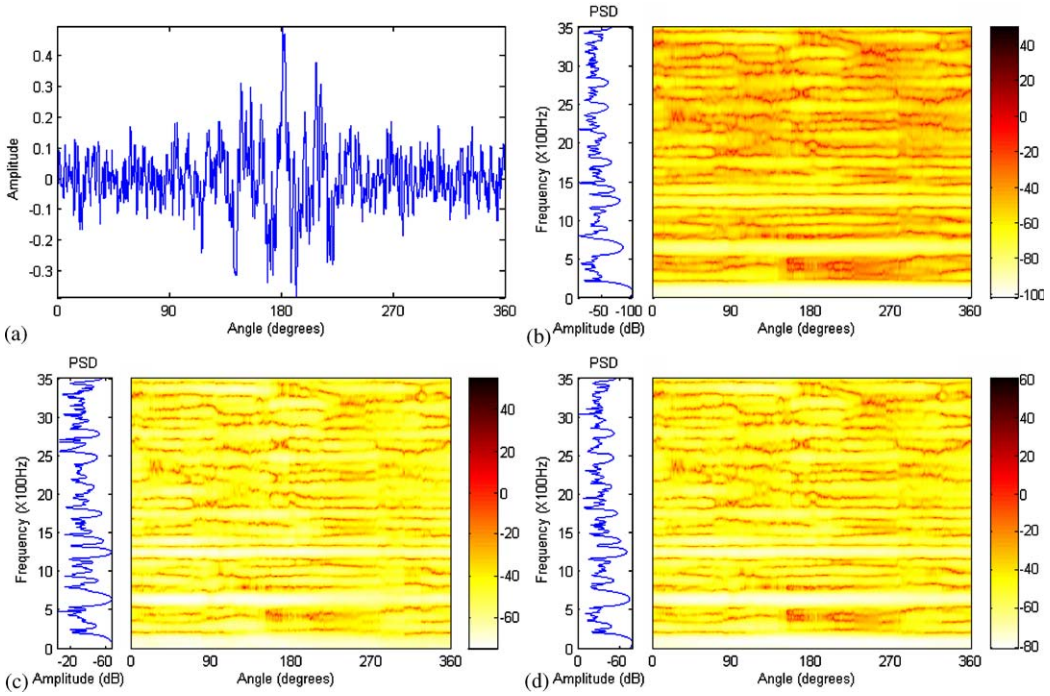

Fig. 15. Residual signal of the driven gear under the faulty state of two non-adjacent broken teeth and T–F maps, where the residual signal is extracted from the TSA signal in Fig. 13(a). (a) Residual signal under faulty state, (b) T–F map of model I (NAKF), (c) T–F map of model II (EKF), (d) T–F map of model III (MEKF).

energy level close to those of the remaining sound part of the driven gear within the entire revolution. This phenomenon confirms the appealing advantages of the proposed parametric models over non-parametric T–F techniques.

5.2.3. *Distributed gear tooth failure (TR#6)*

The test run TR#6 was driven at 300% torque level until eight teeth on the driven gear are broken. Fig. 17(a) is the TSA signal obtained from the second to last data file. An evident amplitude modulation can be recognized within a relatively wider angular interval [110°, 240°] from the TSA trace. The resulting T–F maps are presented in Figs. 17(b)–(d). Strong modulation effects can be observed within the angular interval [110°, 240°] in each T–F map. This result is also well consistent with the findings from the TSA trace in Fig. 17(a).

The T–F analysis by STFT shows that the dominant fault-affected frequency band is [200, 2000] Hz as shown in Fig. 4(g). The cross-section mean plots within the band of [200, 2000] are then calculated and presented in Fig. 18. The cross-section mean plots of the three parametric models present very similar and effective descriptions of the fault-induced feature (CI), as shown

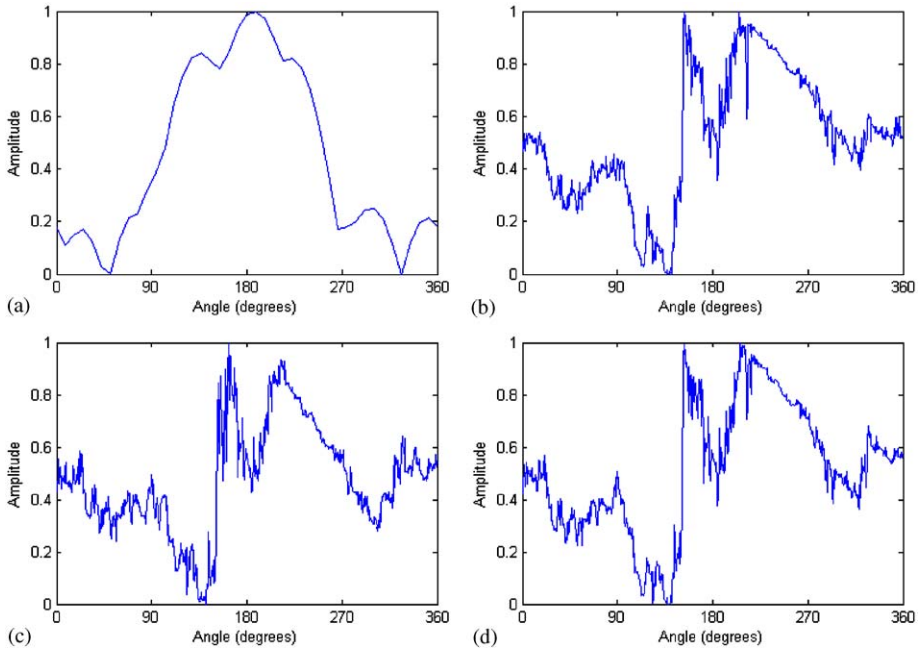

Fig. 16. Normalized cross-section mean plots of STFT and proposed models for the residual signal in Fig. 15(a), where the averaged frequency band is [200, 600] Hz. (a) Cross-section mean of STFT, (b) cross-section mean of model I (NAKF), (c) cross-section mean of model II (EKF), (d) cross-section mean of model III (MEKF).

in Figs. 18(b), (c) and (d), respectively, which are generally consistent with the cross-section mean plot of STFT as shown in Fig. 18(a).

The extracted residual signal is displayed in Fig. 19(a). Apparent amplitude increments are evenly present within [110°, 240°] which clearly indicates the existence of distributed gear tooth damage. On examining Figs. 19(b)–(d), it is found that the resulting T–F maps of all models demonstrate a remarkable consistency. The dominant power region can readily be identified within the angular interval [110°, 240°] from the three maps. This also corroborates well with the visual observation of the residual signal in Fig. 19(a).

Further analysis using STFT reveals that the dominant region which can highlight the existence of fault-induced feature is located in the frequency band [200, 500] Hz as shown in Fig. 4(h). The cross-section mean plots obtained by taking spectral average over this band outline an exactly identical description of the fault-induced effects as shown in Fig. 20 and all methods clearly indicate (CI) the fault-induced feature.

6. Conclusions

This paper presents a thorough and comprehensive investigation of the proposed adaptive parametric models, transformed from time-varying vector-autoregressive model with their

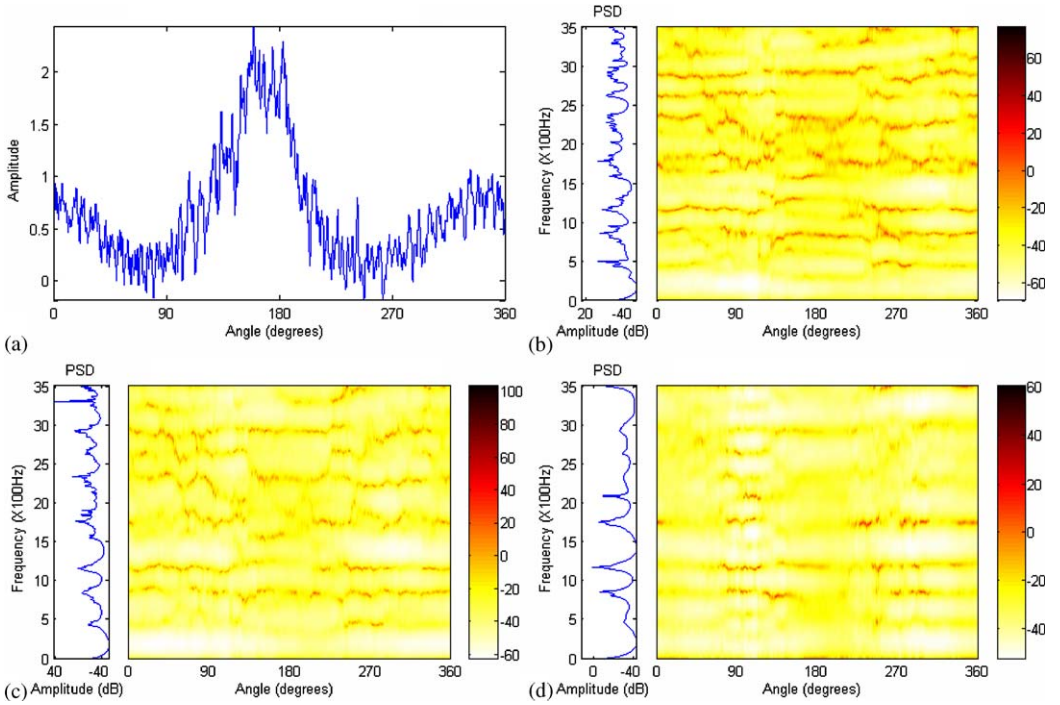

Fig. 17. TSA signal of the driven gear under the faulty state of distributed broken teeth and T–F maps, where the TSA signal is obtained from TR#6, and the number of averaged revolutions is 19. (a) TSA signal under faulty state, (b) T–F map of model I (NAKF), (c) T–F map of model II (EKF), (d) T–F map of model III (MEKF).

parameters estimated by means of advanced Kalman filtering algorithms based on different assumptions of the evolution laws of the state vector, under highly non-stationary conditions using actual gearbox vibration signals. In conclusion, the experiments show that all models are able to produce high-quality T–F representations and clearly highlight the gear fault-induced features in the resulting T–F representations under various states of gearboxes.

In particular, the EKF- and MEKF-based models demonstrate appealing advantages in localizing the gear fault-induced features, while the NAKF-based model demonstrates strong robustness to arbitrary model initializations. However, due to the linearization schemes employed by EKF and MEKF, the white Gaussian assumption of model residuals cannot always be guaranteed for these two models, but it does not reduce the accuracy and resolution of the resulting T–F representations and neither harm the detection of gear fault-induced features in T–F domain provided that appropriate model initialization is performed. This is the reason why the optimality conditions in most experiments of this study are set aside for models II and III in order to above all obtain accurate T–F representation. In this connection, model I is more preferred for automatic condition monitoring.

However, it must be noted that the effectiveness of each proposed model depends on the evolution law assumption of the state vector and also the linearization scheme of the nonlinear

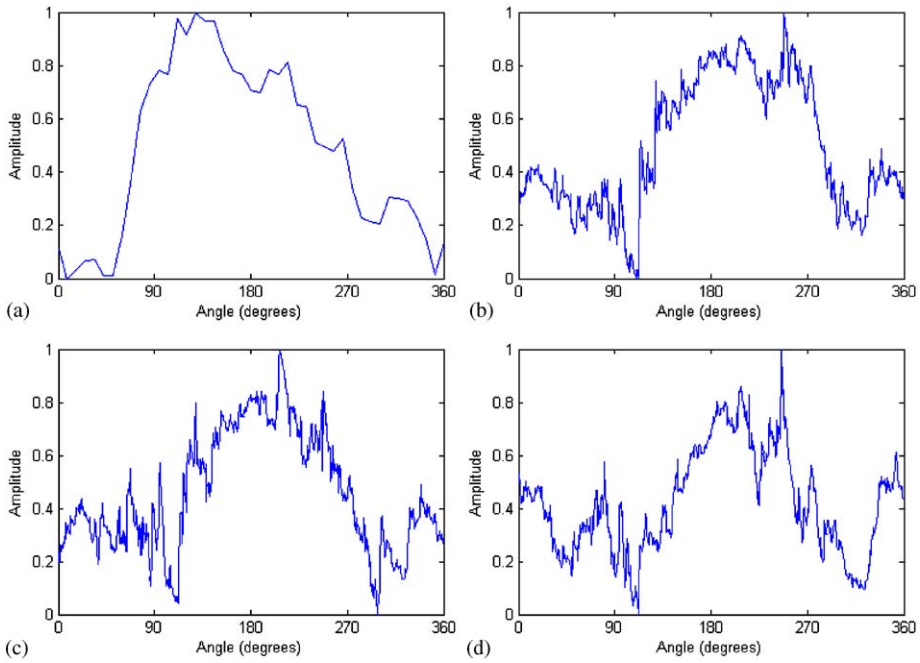

Fig. 18. Normalized cross-section mean plots of STFT and proposed models for the TSA signal in Fig. 17(a), where the averaged frequency band is [200, 2000] Hz. (a) Cross-section mean of STFT, (b) cross-section mean of model I (NAKF), (c) cross-section mean of model II (EKF), (d) cross-section mean of model III (MEKF).

state equation for models II and III. If the assumption and linearization scheme are well consistent with the status of the TSA or residual signal, the resulting T–F representations can be of strong consistency with that of STFT. Here, we assume in advance that STFT is able to provide an acceptable benchmark T–F representation for comparison. It is found in our experiments that models II and III have a greater potential to approximate the true underlying dynamics of a signal only if an appropriate model initialization is offered. Nevertheless, there is no rigorous theory to guarantee the optimality of extended Kalman filter or its advanced derivatives in general since all existing extended Kalman filters are ad hoc schemes with different linearizations. Therefore, adjustment of model parameters might be required especially for models II and III in practical applications.

As well, it is noteworthy that, in comparison with non-parametric T–F methods such as STFT, the proposed parametric models are able to provide much more delicate and precise high-resolution T–F representations. In addition, an adaptive noise estimation mechanism is inherently embedded in the proposed models, which provides an efficient isolation of the true underlying process from noise disturbances, whereas non-parametric T–F methods do not possess such an appealing advantage. However, if sufficient sampling points are available, non-parametric techniques like STFT can achieve any high resolution, although it is still subject to a well-known uncertainty principle. On the other hand, the increase of sampling points will significantly

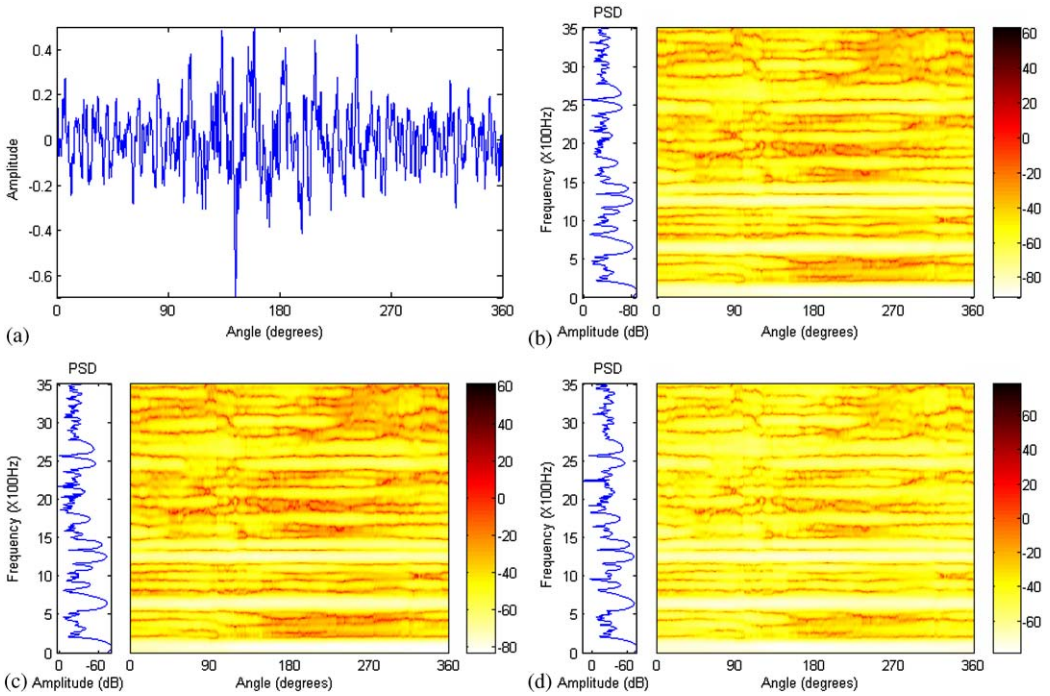

Fig. 19. Residual signal of the driven gear under the faulty state of distributed broken teeth and T–F maps, where the residual signal is extracted from the TSA signal in Fig. 17(a). (a) Residual signal under faulty state, (b) T–F map of model I (NAKF), (c) T–F map of II (EKF), (d) T–F map of model III (MEKF).

aggravate the computational load of parametric models and consequently result in a significant cost of time. In particular, in case that a sufficient removal of noise components from the raw fault signal is obtained by TSA, the adaptive noise estimation function of the proposed parametric models will not play a critical role. In such a circumstance, it is suggested that the computation of parametric T–F representation jump over a constant number of sampling points. This is equivalent to selecting some equally spaced sampling points from a TSA or gear motion residual signal for T–F analysis. As such, the information contained in the skipped sampling points without processing is lost. However, if the angle corresponding to the skipped number of sampling points in one jump is less than that corresponding to the total number of teeth involved in the meshing motion at each time instant, the gear fault-induced impulse can still be more or less retained for parametric T–F analysis. For example, the contact ratio of 2.388 as shown in Table 1 indicates that in average there are 2.388 pairs of teeth are always in contact, which correspond to an angle of 18.69° ($=2.388\times 360^\circ/46$) which in turn indicates 54.56 sampling points ($=18.69^\circ\times 1051/360^\circ$). Thus, a constant signal length of 54 or less sampling points could be skipped in each jump in the TSA or gear motion residual signal. As an alternative approach, a fast computing hardware device is obviously desirable for parametric T–F analysis.

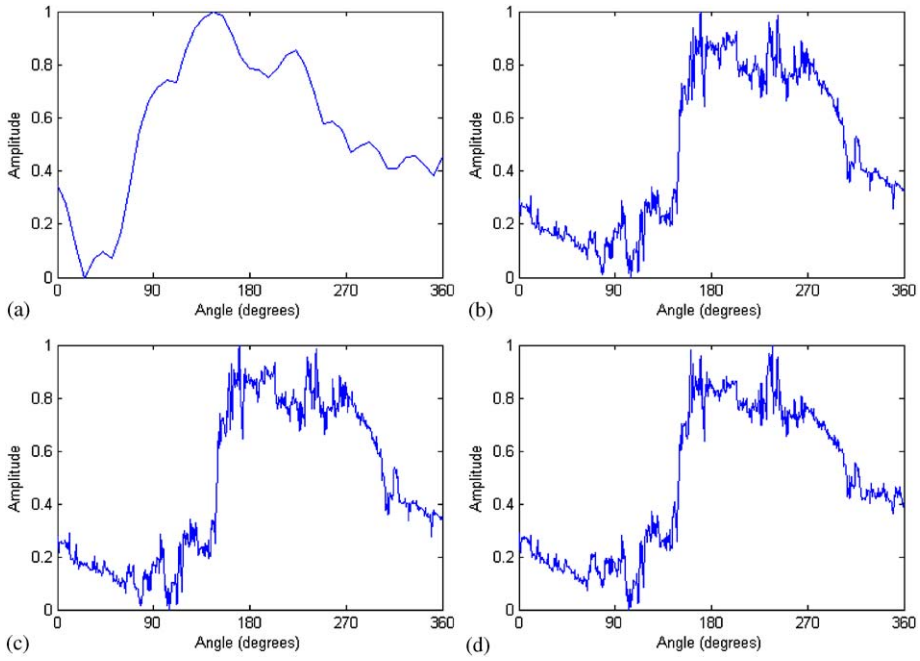

Fig. 20. Normalized cross-section mean plots of STFT and proposed models for the residual signal in Fig. 19(a), where the averaged frequency band is [200, 500] Hz. (a) Cross-section mean of STFT, (b) cross-section mean of model I (NAKF) (c) cross-section mean of model II (EKF), (d) cross-section mean of model III (MEKF).

Acknowledgements

We are most grateful to the Applied Research Laboratory at the Pennsylvania State University and the Department of the Navy, Office of the Chief of Naval Research (ONR) for providing the data used to develop this work. We thank Bob Luby at PricewaterhouseCoopers for his help to obtain the data. The authors also wish to thank the Natural Sciences and Engineering Research Council of Canada (NSERC), Material and Manufacturing Ontario of Canada (MMO) and the CBM Consortium companies for their financial supports. Finally, we appreciate very much the valuable comments from the anonymous referees who greatly helped to improve this work.

References

[1] A.H. Christer, W. Wang, J.M. Sharp, A state space condition monitoring model for furnace erosion prediction and replacement, *European Journal of Operational Research* 101 (1997) 1–14.

[2] J.H. Williams, A. Davies, P.R. Drake, *Condition-based Maintenance and Machine Diagnostics*, Chapman & Hall, London, 1994.

[3] D. Kocur, R. Stanko, Order bispectrum: a new tool for reciprocated machine condition monitoring, *Mechanical Systems and Signal Processing* 14 (2000) 871–890.

[4] Condition-Based Maintenance Department, Applied Research Laboratory, The Pennsylvania State University, MDTB data (data CDs: TR#10, TR#7, TR#8 and TR#6), 1997–1998.

[5] C.S. Byington, J.D. Kozlowski, Transitional data for estimation of gearbox remaining useful life, Mechanical Diagnostic Test Bed Data CDs, Applied Research Laboratory, Condition-Based Maintenance Department, The Pennsylvania State University, 2000.
[6] P.D. McFadden, Examination of a technique for the early detection of failure in gears by signal processing of the time domain average of the meshing vibration, *Mechanical Systems and Signal Processing* 1 (1987) 173–183.
[7] P.D. McFadden, Detecting fatigue cracks in gears by amplitude and phase demodulation of the meshing vibration, *Journal of Vibration, Acoustics, Stress, and Reliability in Design* 108 (1986) 165–170.
[8] W.Q. Wang, F. Ismail, M.F. Golnaraghi, Assessment of gear damage monitoring techniques using vibration measurements, *Mechanical Systems and Signal Processing* 15 (2001) 905–922.